Ocean Systems Engineering, *Vol. 15, No. 2 (2025) 127-152*
https://doi.org/10.12989/ose.2025.15.2.127

Hydrodynamic analysis of an undulating body: Integrating the benefits of rectangular fin and NACA profile

B. Narendhiran[a] and K. Narendran[*]

Department of Ocean Engineering, Indian Institute of Technology (IIT) Madras, Chennai, 600036, Tamilnadu, India

(Received April 25, 2025, Revised May 22, 2025, Accepted May 28, 2025)

Abstract. In general, for an autonomous underwater vehicle (AUVs), its shape is one of an important parameter influencing its performance. AUVs can be propelled using conventional propellers or by undulating (flapping), its body like aquatic animals. Most of the existing AUVs that propels by undulating its body are multi-segmented and rectangular. However, research studies have often focussed on NACA hydrofoils, despite the prevalence of rectangular designs in AUVs. This paper aims to fill the gap in the current research by conducting a comparative study of the thrust force generation and efficiency of rectangular fin and hydrofoil. Besides, a merged body shape (MBS) has been proposed, combining the advantages of hydrofoil and fin. A comprehensive analysis has been made by comparing the performance of an undulating NACA 0012 foil, a rectangular fin with the proposed MBS at St = 0.2 – 1, for non-dimensional wavelengths (λ^*= 0.8 and 1.0) at Re = 1000. Increase in thrust forces are observed with increase in St and λ^*. The efficiency at λ^*=0.8 is higher than that at λ^*=1.0, indicating optimal wavelength for high efficiency. The MBS generates a mean thrust coefficient comparable to the hydrofoil, offering a balance of thrust and modular adaptability.

Keywords: anguilliform; autonomous underwater vehicles; biomimetic; hydrodynamics; undulatory motion

1. Introduction

Through millions of years of evolution, fish species have developed incredible swimming abilities. Intrigued by the remarkable performance of fish, research has been carried out to understand their anatomical structure and swimming dynamics, to exploit those techniques in the field of engineering and technology for the development of Bionic Autonomous Underwater Vehicles (BAUV) in the commercial and research applications (Barrett *et al*. 1996). In laboratory studies of van Ginneken *et al*. (2005) observed that eels undergo anguilliform motion to achieve high swimming efficiency, travelling long distances with remarkably low energy expenditure. During the migration, eels can travel over 5000 kilometres in 180 days (Thillart *et al*. 2007). The energy-efficient swimming techniques employed by undulating aquatic animals, such as eels and lampreys, provide a valuable model for developing autonomous underwater vehicles (AUVs).

*Corresponding author, Assistant Professor, E-mail: knaren.27@gmail.com; knaren@iitm.ac.in
[a]Ph.D. Student, E-mail: dhiran.aero@gmail.com

http://www.techno-press.org/?journal=ose&subpage=7 ISSN: 2093-6702 (Print), 2093-677X (Online)

Table 1 Existing Literature on various profile shapes

Investigators	Profile	A_{max}	St	λ^*	Re	Approach
Kern and Koumoutsakos (2006)	Eel Shape	0.11 & 0.14	0.67 & 0.59	-	2400–3900	Numerical
Borazjani and Sotiropoulos (2009)	Lamprey shaped	0.1	0-1.2	0.95	300, 4000, and ∞	Numerical
Abbaspour and Ebrahimi (2015)	NACA 0012	0.2	0.05, -2.5	1	40000	Numerical
Zhang *et al*. (2018)	NACA0004 ,0008, 0012, 0016, 0020, & 0024	0.125	0.06 – 0.27	1	50, 500, 1000, 5000, 10^4, 5x10^4, 10^5 & 2x10^5	Numerical
Thekkethil *et al*. (2018)	NACA0012	0.1	0.2-0.7	0.8-8 and ∞	5000	Numerical
Khalid *et al*. (2020)	NACA0012	0.1	0.1-0.8	0.5-1.5	10^2, 10^3, & 5x10^3	Numerical
Khalid *et al*. (2021)	Eel	0.1	0.3 and 0.4	0.5 to 1.25	3000	Numerical
Gupta *et al*. (2021a)	NACA0012	0.1	-	0.8 - 8 and ∞	50, 500, & 1500	Numerical
Gupta *et al*. (2021b)	NACA0012	0.1	0 - 1.2	-	500, 1000, 2000, & 5000	Numerical
Gupta *et al*. (2022)	Anguilliform (NACA0006,0008)	0.1	0.6	0.65 to 1	5000	Numerical
	Carangiform (NACA0012,0018, 0024)	0.1		1.0 to 0.65		

A_{max} =Non-dimensional maximum amplitude, St = Strouhal number, λ^* = Non-dimensional wavelength of undulation and Re = Reynolds Number

The freestream flow over an undulating body is governed by several non-dimensional parameters: the Reynolds number (Re), the Strouhal number (St), the non-dimensional maximum amplitude (A_{max}), and the wavelength of undulation (λ^*), defined as follows

$$Re = \frac{UL}{\nu} \; ; St = \frac{2Af}{U} \; ; A_{max} = \frac{A}{L} \; ; \lambda^* = \frac{\lambda}{L} \tag{1}$$

Where υ is the kinematic viscosity of the fluid, U is the free-stream velocity of the flow, L is the chord length (length) of the foil (fin), A is the maximum amplitude of undulation (typically observed at the tail), and f is the frequency of undulation.

Research by Barrett *et al*. (1999) highlighted that undulating bodies experience lower drag, consume less power, and consequently operate with greater energy efficiency. The Table 1 provides a compilation of different studies investigating various body shapes and their operating conditions. Borazjani and Sotiropoulos (2009) numerically investigated the hydrodynamics of a lamprey-like flexible body, providing tremendous insight into how undulatory motion reduces drag forces. According to their findings Re and St are the primary parameters determining the hydrodynamic performance, and the anguilliform swimmers attain high propulsive efficiency (η) at lower Re (4000). The propulsive efficiency (η) is the ratio of thrust power to input power.

It is a common practice to employ symmetric NACA foils as a representation of a fish body due to their simplicity compared to modelling an actual fish shape. Abbaspour and Ebrahimi (2015) numerically compared the thrust, lateral force, power consumption, and efficiency of a NACA0012 profile under flapping and undulation motion for a range of St to understand the

(a) AmphiBot I
(Crespi *et al*. 2005)

(b) AmphiBot II
(Crespi and Ijspeert 2006)

(c) AmphiBot III
(Porez *et al*. 2014)

Fig. 1 AmphiBot

(a) The Lamprey Robot
(Stefanini *et al*. 2012)

(b) Salamandra robotica II
(Crespi *et al*. 2013)

(c) Envirobot
(Bayat *et al*. 2016)

Fig. 2 Undulatory robots

efficiency of the body motion. Their results showed that the flapping motion generates a much higher thrust force with a high-energy requirement compared to the undulation mode of motion. Thekkethil *et al*. (2018) conducted numerical investigations on NACA0012 profile subjected to undulatory and pitching motion for a range of *St* (0.2-0.7) and *Re* = 5000.

The results showed that undulation motion require less energy for propulsion when compared to pitching motion thereby generating higher propulsive efficiency. Zhang *et al*. (2018) numerically investigated the effect of *Re* and foil thickness on the η by considering a wide range of *Re* (50 to $2x10^5$). For assessing the effect of thickness, six different NACA profiles (NACA0004, 0008, 0012, 0016, 0020, and 0024) were investigated. They observed that the *Re* is directly proportional to the thrust force and propulsive efficiency up to *Re*=$5x10^4$ and becomes asymptotic beyond that. They reported that thin foils generate higher thrust force, but exhibit poorer propulsive efficiency when compared to thick foils. Khalid *et al*. (2020) analyzed the hydrodynamic performance of undulating swimmers using NACA0012 foil for a range of *Re* (10^2,10^3, & $5x10^3$), *St* (0.1 – 0.8), and non-dimensional undulating wavelength (λ^*) (0.5-1.5). They reported that anguilliform swimmers have high η at low speeds (*Re* =10^2). Anguilliform species employ undulation motion with undulation wavelength (λ) shorter than their *BL* (Khalid *et al*. 2021). They investigated this phenomenon through 3D numerical simulation, considering an eel-shaped body, by altering the *St* (0.3 and 0.4) and λ^* (0.5 to 1.25 at intervals of 0.15) at *Re*=3000. Their findings indicate that the thrust and drag forces increase for higher λ^*, which is not desirable except during escape manoeuvres. The anguilliform species achieves high efficiency when they swim at $\lambda^* \sim 0.8$. Anguilliform swimmers exhibit burst-and-coast (B&C) swimming mode and continuous swimming mode (Kern and Koumoutsakos (2006) and Gupta *et al*. (2021a). From their numerical studies, they reported that B&C swimming mode consumes higher energy compared to the continuous swimming mode. Gupta *et al*. (2021b) reported that undulatory body exhibits higher η at the condition when the phase velocity, $c = \lambda/T$, exceeds the *U* for NACA0012 profile. Furthermore, Gupta *et al*. (2022) conducted a detailed investigation on switching effect of swimming modes (between anguilliform and carangiform) and shape effect (various NACA

profiles). They reported that when carangiform kinematics is imposed to an anguilliform fish body the thrust force increases with decrease in η, which is attributed to the phenomenal increase in power input to generate higher thrust power. However, if the conditions are reversed the opposite happens.

To the best of authors' knowledge, most of the numerical studies were conducted to investigate undulatory swimming mode for NACA 00XX profiles due to its simplicity in modelling and analysis. In reality, the undulatory AUVs are usually designed as rectangular shapes rather than a NACA profile. The body shape of AUVs is one of a critical parameter in reducing drag forces and achieving higher efficiency simultaneously. Undulating swimmers such as eels, have long-streamlined body that minimizes drag force and reduces energy expenditure while travelling over long distances.

Undulatory AUVs are modular by design, which can be scaled up/down in sizes, enabling it to move seamlessly through narrow or irregular spaces, climb over obstacles, or manoeuver in environments with ease compared to conventional AUVs. On this aspect, the amphibious robots, such as AmphiBot I, II, and III, developed by Crespi *et al*. (2005), Crespi and Ijspeert (2006), Porez *et al*. (2014), are capable of performing undulatory motion, as shown in Figs. 1(a, b and c) respectively. The lamprey robot, inspired by a lamprey, is depicted in Fig. 2(a). Additionally, the Salamandra robotica II, developed by Crespi *et al*. (2013) and inspired by a salamander, can perform both swimming and crawling, as illustrated in Fig. 2(b). The Envirobot, as shown in Fig. 2(c) developed by Bayat *et al*. (2016), further expands on bio-inspired locomotion strategies. These devices are multi-segmented that move in wave-like pattern resembling anguilliform locomotion. Each segment may accommodate control mechanisms/motors/sensors/etc. In general, these devices resemble like a rectangular fin, which consist of uniform thickness all along the length of its body, unlike NACA profiles, where the thickness varies. As discussed above, most of the existing undulatory AUVs has uniform thickness body shape like a rectangular fin with or without tail. However, research studies have often focused on symmetric NACA hydrofoils due to their resemblance to a simplified fish body, even though rectangular designs are more commonly used in AUVs. This motivated the authors to bridge the gap and exploit the hydrodynamic benefits of NACA profile at the same accommodate the modules/segments. Based on this we propose a body profile that has the benefits of both hydrofoil and fin. In this article, we are proposing a merged body shape (MBS) of NACA profile and rectangular fin to accommodate the control mechanisms/motors/sensors at the same time without compromising on the efficiency and drag reduction. Followed by the hydrodynamic analysis have been conducted by comparing the performance of an undulating NACA 0012 foil, a rectangular fin with the MBS.

2. Method

2.1 Problem description

A schematic flow configuration over the deformed NACA0012 hydrofoil (herein after referred to as foil) is shown in Fig. 3. Positioned in an x-directional uniform flow of velocity U, with the foil's leading edge at the Cartesian coordinate system's origin. L, being the chord length of the foil.

The conventions used throughout the paper are illustrated in Fig. 3, where the leading edge is referred to as the "head," and the trailing edge as the "tail." The foil is shown deformed about the symmetry line (chord line), with the top of the foil designated as the "right side" and the bottom as

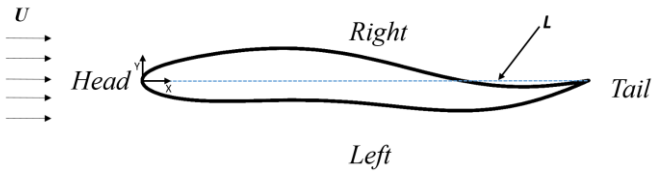

Fig. 3 Schematic flow configuration over the deformed NACA0012 hydrofoil

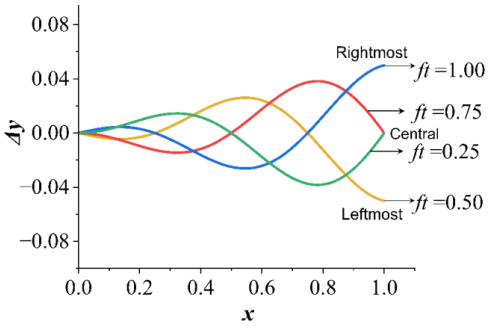

Fig. 4 Undulating motion of the chord line of foil at four positions during its cycle for $\lambda^* = 1.0$

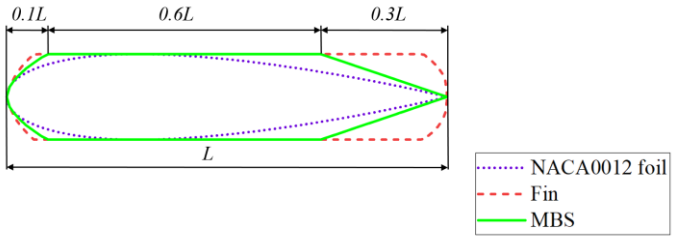

Fig. 5 MBS- a blend of NACA0012 hydrofoil and rectangular fin

the "left side." In this work, the tethered model (TM) approach is implemented. The TM approach is equivalent to moving an undulating body through fluid, wherein a tether ensures zero net instantaneous force on the body, either by absorbing the extra thrust or providing sufficient force to overcome the drag, allowing the undulating body to move forward at a constant velocity. Both the incoming velocity (U) and the lateral undulating velocity (v_y) serve as the primary input parameters governing the TM simulation (Thekkethil *et al*. 2018, Wei *et al*. 2022). Here the foil is considered as rigid (no flow induced deformation). The lateral body deformation (Δy) of the mid line of the foil (Videler and Hess 1984), as a traveling undulatory motion, given below

$$\Delta y = A(x)\, sin(\frac{2\pi x}{\lambda} - 2\pi f t) \quad (2)$$

Where $A(x)$ is the amplitude of the foil motion which is linearly increasing along the lateral direction from $x=0$ *to* $x=L$, λ is the wavelength of the traveling wavy motion over the body, f is the

Table 2 Non-dimensional governing parameters considered in the current study

St	*Re*	λ^*	A_{max}
0.2-1(ΔSt=0.2)	1000	0.8 & 1.0	0.05

frequency of undulatory motion (f = 1/T, where T is undulation time period) and t is the instantaneous time. For anguilliform motion, the amplitude attains the maximum value at the tail (x=L). The undulation motion of the chord line of the foil at four distinct time instants for λ^* = 1.0 is depicted in Fig. 4.

In this study, MBS is developed based on the research by Jellyman (1979), Borazjani and Sotiropoulos (2009) on anguilliform fish species such as eels and lampreys, featuring a smoothly tapered head, a nearly uniform mid-section that constitutes about 70-80% of the body length, and a small, streamlined tail section. This structure resembles a combination of a symmetric foil and a rectangular shape. This shape effectively combines the benefits of both foil and rectangular fin designs. The foil considered is NACA0012 foil with chord length of L and the rectangular fin with semi-circular head and tail section of radius (6% of the total length) and midsection is of uniform thickness with length (88% of the total length). The proposed shape (MBS) is shown in Fig. 5. This design includes a constant-thickness mid-section (60% of the total length), like rectangular fin, which allows for the integration of standard modules found in existing undulatory AUVs. It also features a triangular tail (30% of the total length) and a smoothly tapered head (10% of the total length) resembling a foil.

3. Numerical approach and validation study

3.1 Numerical approach

Here, the transient fluid flow conditions around the body is simulated using the CFD software Ansys-Fluent 2023R1. The fundamental equations governing unsteady, incompressible flow for a Newtonian fluid consist of the conservation equations for mass and momentum as shown in Eqs. (3) and (4), respectively.

$$\nabla . u = 0 \tag{3}$$

$$\frac{Du}{Dt} = -\frac{1}{\rho}\nabla p + \upsilon \nabla^2 u \tag{4}$$

Where u is the velocity vector, p is the static pressure, ρ is the density and υ is the kinematic viscosity of the fluid.

The spatial discretization of the Navier–Stokes Eqs. (3) and (4) is accomplished using the finite-volume method. To address the challenge of handling unsteady flow problems, the Pressure-Implicit with Splitting of Operators (PISO) scheme is implemented to achieve pressure-velocity coupling. This approach is chosen due to its effectiveness in managing such flow scenarios (Ji and Huang 2017). In the spatial domain, a second-order accuracy discrete format is employed to discretize the convection term. For temporal discretization, a first order implicit scheme is utilized to discretize physical time. The four equations turbulent transition SST model (Sun *et al*. 2020) is adopted and the maximum y+ value found to be less than 0.5 for the chosen

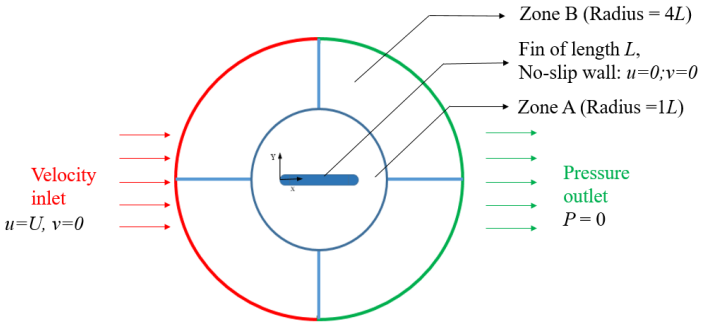

Fig. 6 Computational domain around the fin

first layer height. The average y+ value for the foil surface is 0.19. So, the numerical parameters considered is sufficient to resolve the boundary layer.

In the computational domain, the displacement of the foil is facilitated by a dynamic grid scheme integrated into FLUENT. During each time step, the motion of the foil is calculated using Eq. (2), while the cells surrounding the foil undergo regeneration and smoothing processes through the utilization of the FLUENT DEFINE_GRID_MOTION function. To maintain the quality of mesh while the body is undergoing undulatory motion, a combination of spring-based smoothing and local remeshing techniques are employed. This approach ensured the validity of the dynamic mesh which is crucial for prescribing wave-like motion patterns (Xiao *et al*. 2011, Ji and Huang 2017, Sun *et al*. 2020, Chao *et al*. 2022).

3.2 Computational domain

The computational domain employed for simulating flow-past an undulating body is represented in Fig. 6. The length (chord) of the fin (foil) is L, is being positioned inside the computational domain, which comprises of two zones, namely A and B. The inner zone (zone A) is in the shape of a circle of radius $1L$ comprises of unstructured triangular elements which aids in mesh motion to realize the undulatory motion of the foil. The outer zone (zone B) of radius $4L$, comprises of structured quadrilateral elements. The inlet boundary condition corresponds to velocity inlet with a uniform free stream velocity ($u=U$, $v=0$). The boundary condition for the surface of the fin is set as no-slip ($u=0$, $v=0$) and the pressure outlet boundary condition is applied at outlet boundary. The computational mesh around the foil, fin and MBS are shown in Figs. 7(a), 7(c) and 7(e).

To accurately capture viscous forces on the body wall, the inflation layers were limited to six. The first layer is located at an average vertical distance of $3\text{x}10^{-3}L$ from the body surface as shown in Figs. 7(b), 7(d) and 7(f). The time step chosen as $(1/1000)^{\text{th}}$ of undulation period (Sun *et al*. 2020, Ji and Huang 2017).

Domain independence studies are conducted by considering, three different domain sizes by varying the radius of inner and outer zones: D1 ($0.51L$ & $2L$), D2 ($1L$ & $4L$) and D3 ($2L$ & $6L$) respectively. These studies are conducted at Re =1000, St =0.8 and λ^* =1.0. The percentage difference for domain radius relative to the largest radius is 1.09% for C_{Tm} and 3.6% for C_{Lrms} on D1. This difference decreases to 0.24% for C_{Tm} and 1.2% for C_{Lrms} on D2. Consequently, a domain size of $1L$ & $4L$ (D2) is considered to be suitable to conduct further studies. Figs. 8(a) and 8(b)

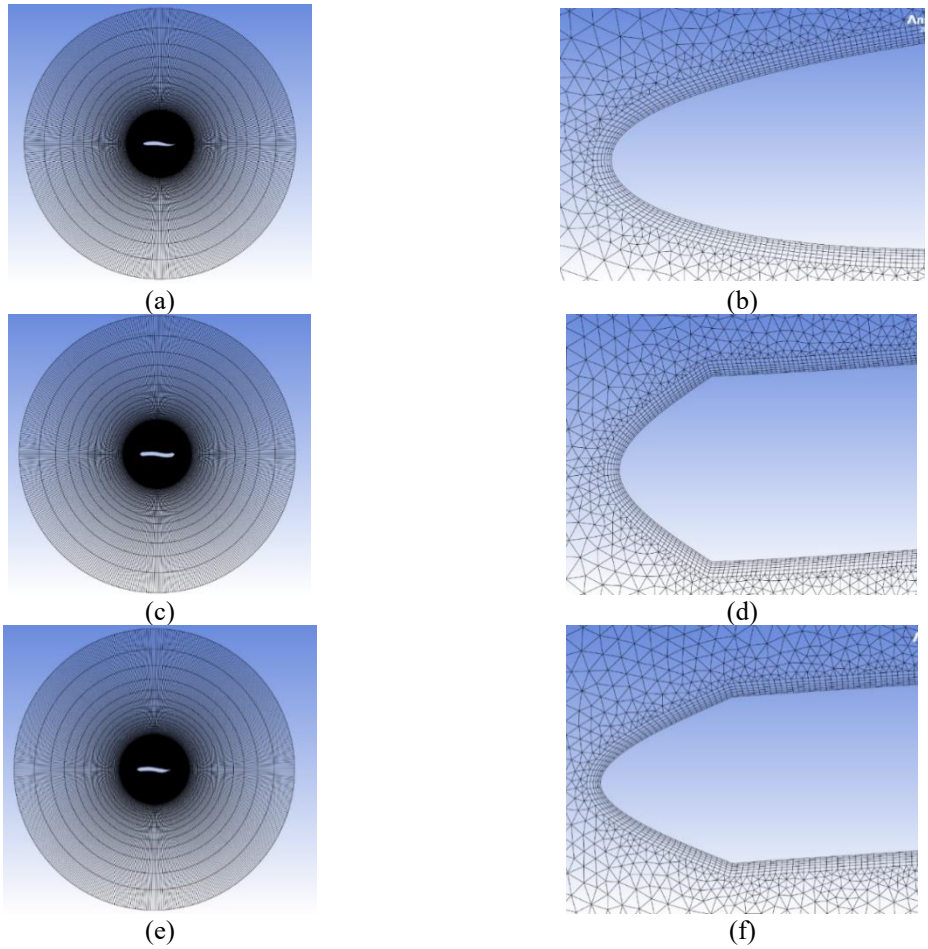

Fig. 7 Computational mesh: Overall view (a), (c) and (e) and zoomed view (b), (d) and (f) showing the mesh around the foil, fin and MBS respectively

presents the time histories of thrust and lateral force coefficients for all the three domains as a qualitative comparison.

3.3 Mesh independence and validation

Mesh convergence test are performed using three different grid numbers: 43358 (M1, coarse), 51374 (M2, medium) and 60927 (M3, fine) corresponding to 314, 679 and 1359 points on the surface of the foil respectively. The tests were validated for Re=1000, St=0.8, λ^* =1.0 and A_{max} =0.05. The time histories of the thrust and lateral force coefficients are shown in Figs. 9(a) and 9(b) respectively for the three different meshes. The percentage difference for coarse mesh relative to the fine mesh is 1.07% for C_{Tm} and 0.05% for C_{Lrms}. This difference decreases to 0.07% for C_{Tm} and 0.02% for C_{Lrms} on medium mesh. Therefore, the medium mesh (M2, 51374 cells) is considered to be appropriate for further studies since its flow field structure is close to that of fine mesh but finer than that of coarse mesh.

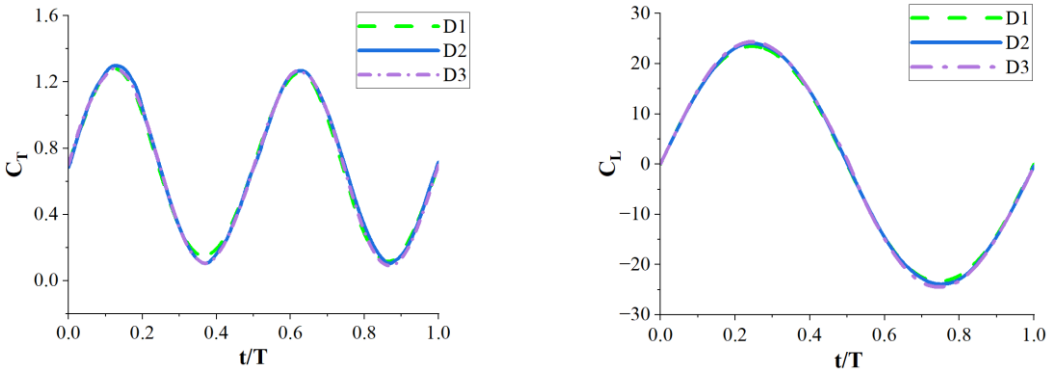

(a) (b)

Fig. 8 Time histories of (a) thrust force coefficients and (b) lateral force coefficients for 3 different domains

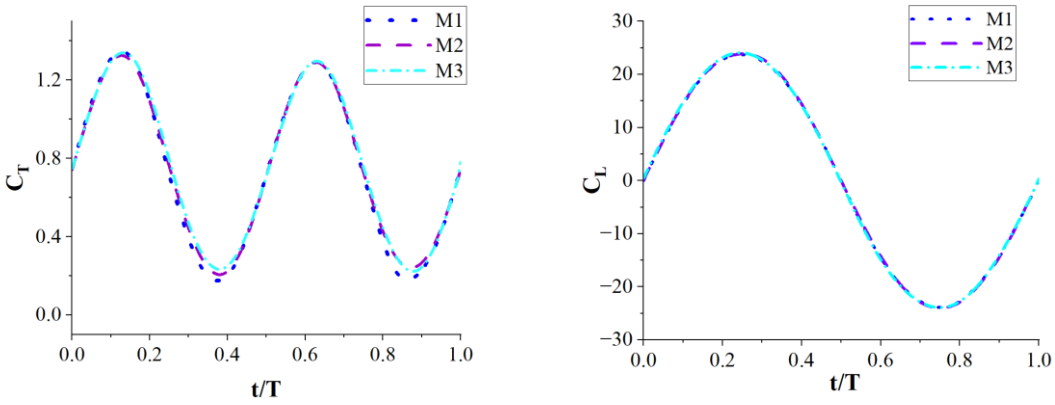

(a) (b)

Fig. 9 Time histories of (a) thrust coefficient (C_T) and (b) lateral force coefficient (C_L) for 3 different grids

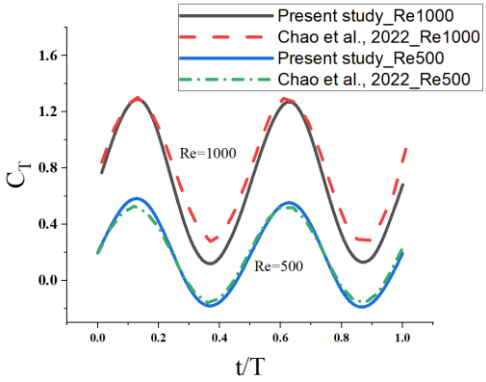

Fig. 10 Comparison of thrust co-efficient against non-dimensional time between present and published results

3.4 Numerical approach validation

The present numerical approach was validated by comparing the time histories of thrust force coefficients with the published work of (Chao *et al*. 2022), as shown in Fig. 10.The foil section employed was NACA0012 and two different parameters considered for validation study: case (i) Re=500, *St*=0.6 and case (ii) *Re*=1000, *St*=0.8 at A_{max} =0.05 and λ^*=1. The comparison reveals that the difference between the published and present work is 1.33% for case (i) and 1.25% for case (ii). This indicates that the computational methods employed in this study are reliable.

4. Results and discussions

To examine the influence of shape on the hydrodynamic performance of the fin, foil, and MBS, the time-averaged thrust and lateral force coefficients were calculated. This was done by varying the Strouhal number (*St*) from 0.2 to 1 in increments of 0.2, using two different undulation wavelengths (λ^* = 0.8 and 1.0) at a constant Reynolds number (*Re* = 1000) and maximum amplitude (A_{max} = 0.05). Undulating motion is typically observed in slow-moving swimmers, with the wavelength of undulation usually shorter than the body length. Many undulating fish species exhibit this behaviour, swimming at low to moderate speeds (Videler and Wardle 1991). In this study, two wavelengths, 0.8 and 1.0 were selected. The wavelength of 0.8 reflects the characteristics of these fish, while the wavelength of 1.0 was chosen to examine how undulation behaves when the wavelength approaches the swimmer's body length. A moderate Reynolds number of 1000 is adopted, consistent with the typical swimming speeds of undulating fish.

In the current 2D comparative numerical study, the hydrodynamic characteristics on the foil, fin and MBS correspond to lateral force (F_L) and thrust force (F_T). The instantaneous coefficients of lateral and thrust forces are given as follows

$$C_L = \frac{F_L}{0.5\rho U^2 L} \quad , \quad C_T = \frac{F_T}{0.5\rho U^2 L} \quad , C_{Tm} = \frac{1}{T}\int_t^{t+T} C_T \, dt \quad , C_{Lrms} = 0.707^* \, C_{Lmax} \tag{5}$$

Where C_L and C_T corresponds to the instantaneous lateral force and thrust coefficient, C_{Tm} is the time averaged thrust coefficient, C_{Lrms} is the RMS value of C_L and C_{Lmax} is the maximum value of C_L in one undulation period

The power consumption of an undulating foil to produce thrust arises from two main components. The first is the power required to drive the undulatory motion of the foil itself, denoted as P_S. This represents the energy expended to sustain the oscillatory movement. The second component is the power needed to overcome drag and generate thrust, denoted as P_T. This accounts for the energy required to counteract resistive forces in the fluid while producing the forward thrust necessary for propulsion (Dong and Lu, 2005, Chao *et al*. 2022, Sun *et al*. 2020).

The power consumption for undulating motion per unit time is defined as

$$P_S = - \oint \left(f_y^p + f_y^f\right) v_y \, ds \tag{6}$$

$$P_T = - F_P U = F_T U \tag{7}$$

where $\oint$ is the integration of the surface of undulating body, the negative value of pressure gradient force (F_P) in the *x*-direction is considered as thrust, since the friction drag doesn't contribute to thrust (Liu and Kawachi 1999). Since the foil is moving in lateral direction, v_y is the

time derivative of lateral displacement (Δy, refer Eq. (2)).

The pressure gradient force component, f_y^p and the friction force component, f_y^f along the lateral undulating direction expressed as

$$f_y^p = -p \tag{8}$$

$$f_y^f = \mu\,[2\,(\frac{\partial v}{\partial y}) - (\frac{dy}{dx})(\frac{\partial v}{\partial x} + \frac{\partial u}{\partial y})] \tag{9}$$

where p is the averaged pressure, u and v are the velocity components in the x and y directions, respectively.

The propulsive efficiency of the undulating body is defined as the ratio of the thrust generated to the power consumed, calculated on a time-averaged basis.

$$\eta = \frac{P_T}{P_S+P_T} = \frac{C_T}{C_S+C_T} \tag{10}$$

The non-dimensional form of P_T and P_S can be expressed as

$$C_T = \frac{P_T}{0.5\rho U^3 L} \text{ and } C_S = \frac{P_S}{0.5\rho U^3 L} \tag{11}$$

4.1 Vortex formation and shedding mechanisms

When the body undulates in a fluid with a travelling wave backward across the body, fluid is pushed on one side (the pressure side) and pulled on the other side (the suction side) with increasing amplitude from head to tail, pushing the fluid downward along its length generating propulsion force (Muller *et al*. 1997). Similarly, as the body undulates laterally (y-direction) from right to left side, it pushes the fluid in the left side, causing a deceleration in the flow. Simultaneously, the flow over the right side experiences suction resulting in acceleration of the fluid. This difference in velocity of the flow between the right and left side of the foil results in vortex formation.

The instantaneous behaviour of vortices is analysed after the flow reaches a state where the flow field and forces around the foil exhibit periodic behaviour in response to its undulatory motion. In this state, vortex shedding, wake structures, and other flow features consistently repeat over each cycle of the foil's motion. This condition, known as the dynamic steady state.When the flow reaches dynamic steady state the instantaneous temporal variation in vorticity of the foil at St=1.0, λ*=0.8, Re=1000 and A_{max}=0.05 is illustrated in Fig. 11. When the foil is decelerating at its rightmost point as shown in Fig. 11(a), resulting in a flow accelerates from left to right side of the foil, near the tail. This creates a difference in velocity along the either sides of the tail tip, resulting in generation of counter-clockwise (CCW) or positive vortex, known as stopping vortex (labelled *Vortex-stop* in Fig. 11(a)). Besides there is formation of an additional vortex referred to as secondary vortex (*Vortex-sec*) [shown inside the oval dotted region in Figs. 11(a)-11(h)] on either side of the foil. The backward traveling wave velocity is represented by U_{wave}= 8.0 [$U_{wave} = f\lambda/U = \lambda^* St/2A_{max}$] (Videler and Hess (1984) and Thekkethil *et al*. 2018), which is significantly higher than the incoming free-stream velocity, therefore the fluid on either side of foil's surface cannot match with the higher traveling wave velocity, which results in the formation of secondary vortex. Moreover, if observed closely (zoomed-in view picture of Fig. 11(c)), a thin layer of CW

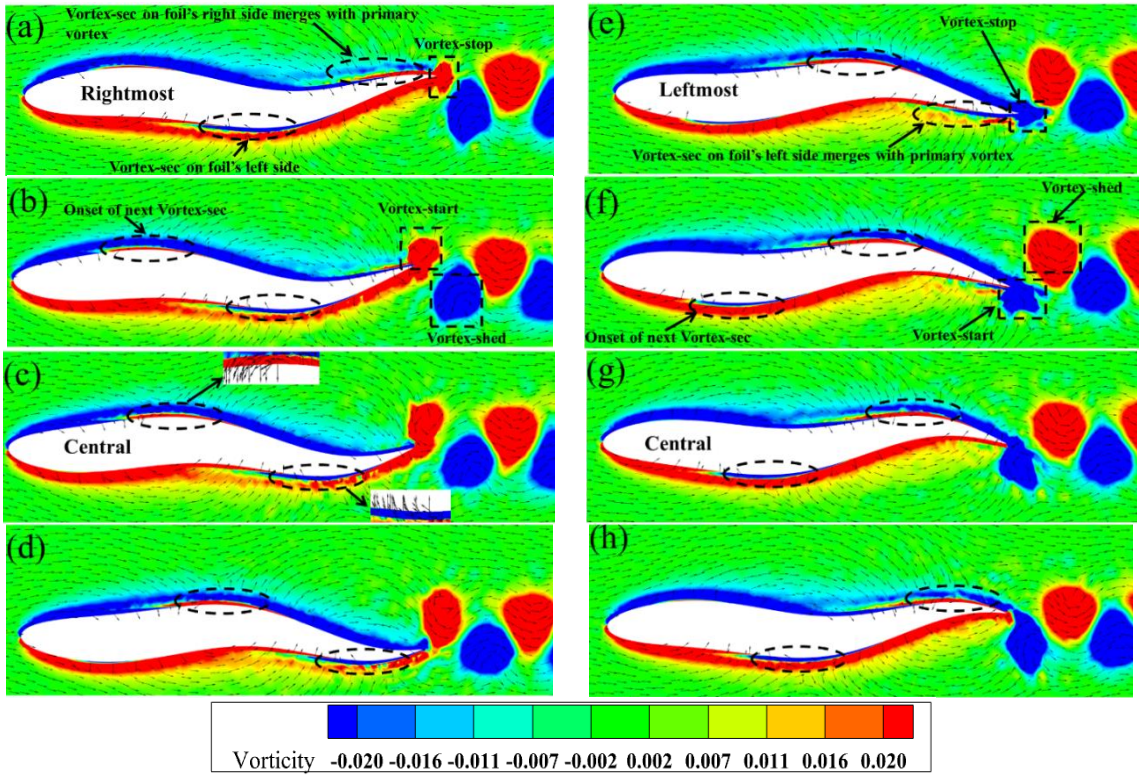

Fig. 11 Instantaneous vorticity contours and velocity vectors at λ^*=0.8 within one period of undulation for foil at Re =1000, St =1.0 and A_{max}=0.05

secondary vortex on the body surface at left side of the foil is surrounded by the CCW primary vortex. Similar, observation is made in the right side of the foil, i.e., the formation of a CCW secondary vortex is enclosed by CW primary vortex. Due to the backward travelling wave motion, the CCW (CW) secondary vortex is advected along the right (left) surface of the foil, with the primary vortex moving in the opposite direction, respectively. The secondary vortex reaches the tail when the foil arrives at its rightmost position, as shown in Fig. 11(a), and merges with the *Vortex-stop* (CCW primary vortex) as the foil begins its leftward motion. As the foil changes its direction by moving towards the left, the pressure difference at the tail, and the merging of secondary vortices cause the initial CCW *Vortex-stop* to grow, now referred to as the starting vortex (*Vortex-start*), as seen in Fig. 11(b). Therefore, the starting vortex is a combination of *Vortex-sec* and *Vortex-stop*. As the foil moves from the rightmost to the leftmost position, it can be observed the stretching and the advection process of *Vortex-start* from tail tip to downstream side, as shown in the Figs. 11(b)-11(e).

The vortex detaches from the foil only when it switches direction back towards the right side of the foil (Fig. 11(f)), transforming the *Vortex-start* (Fig. 11 (b)) into a *Vortex-shed* (Fig. 11(f)). The *Vortex-start* continues to grow until the foil reaches the rightmost position, at which point it is detached by the generation of a *Vortex-stop*. Consequently, the vorticity contours in Figs. 11(a)-11(h) demonstrate that CCW (CW) vortex form on the foil's left (right) side and shed on its rightmost (leftmost) side. A similar pattern was reported by Thekkethil *et al*. (2018). This

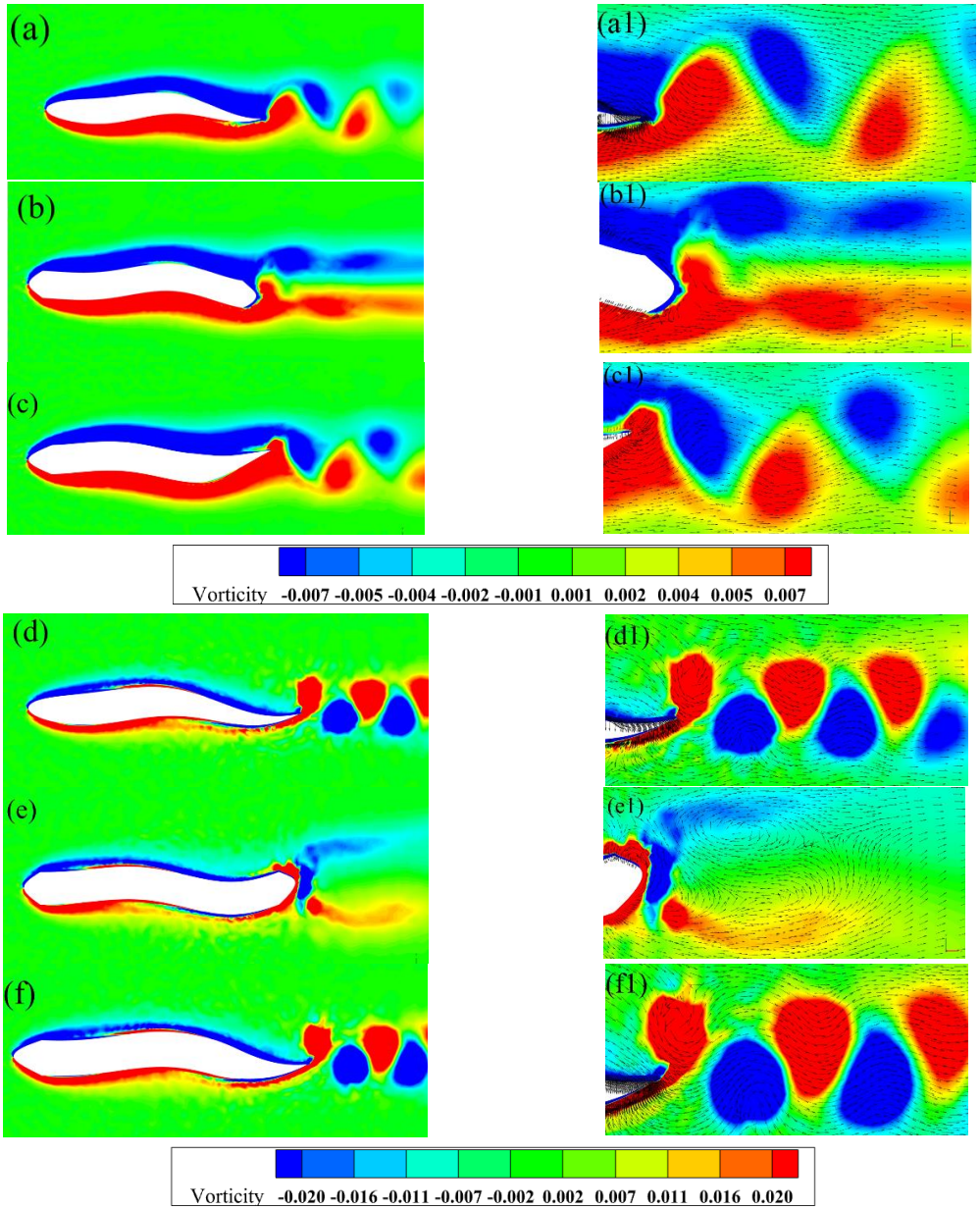

Fig. 12 Instantaneous vorticity contours and velocity vectors at λ*=0.8: (a)-(c) represents vorticity contours of foil, fin and MBS at *St*=0.2. (d-f) represents vorticity contours of foil, fin and MBS at *St*=1.0. (a1)-(c1) represents velocity vectors (zoomed-in view) near the wake of foil, fin and MBS at *St*=0.2. (d1)-(f1) represents velocity vectors (zoomed-in view) of near the wake of foil, fin and MBS at *St*=1.0 for *Re*=1000 and A_{max} = 0.05

alternating shedding pattern, in which vortices reverse positions from one side of the foil to the other as they grow and shed, results in the characteristic reverse von Kármán vortex street. A jet flow forms between the consecutive vortices, creating momentum excess that generates positive thrust force.

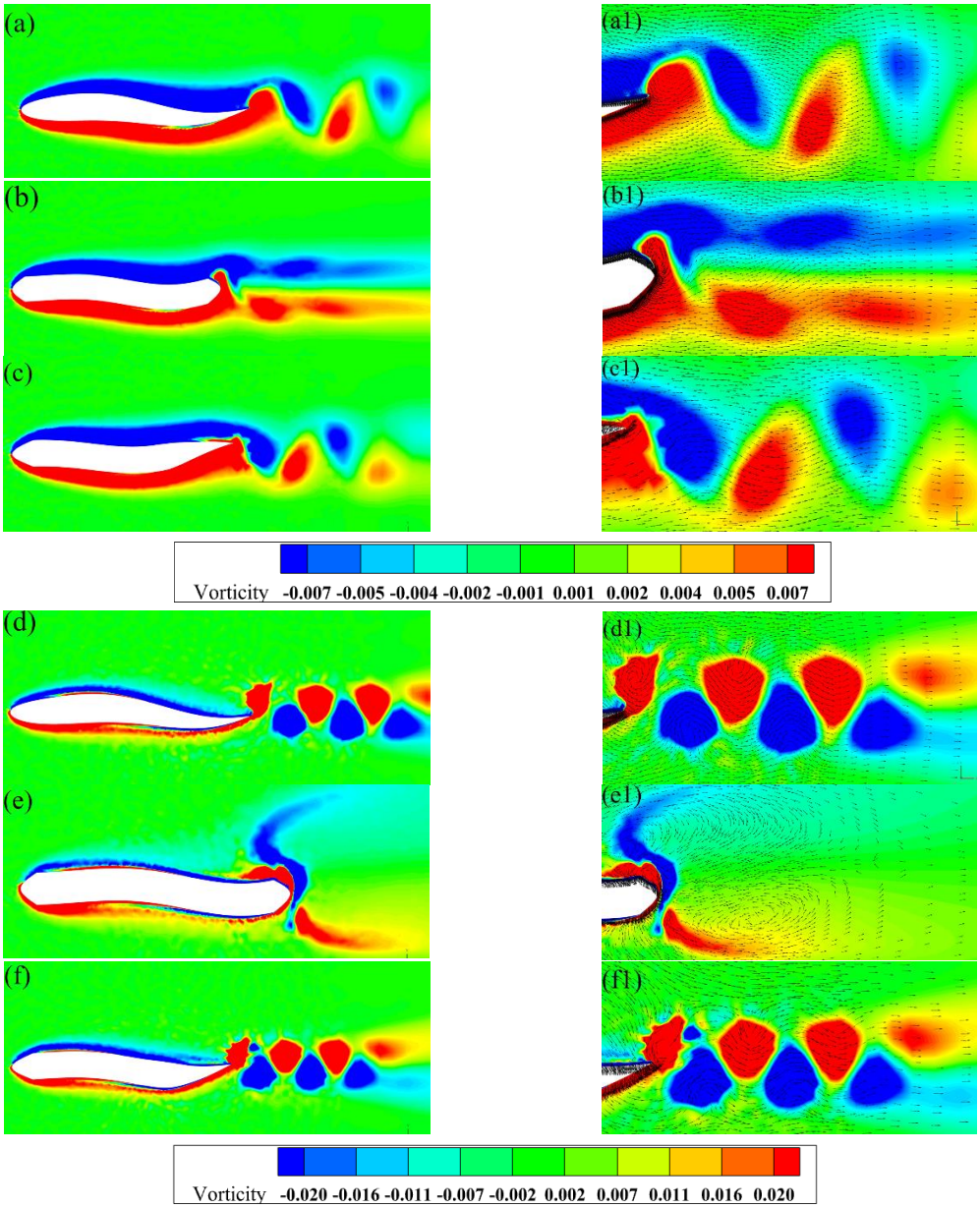

Fig. 13 Instantaneous vorticity contours and velocity vectors at λ^*=1.0: (a)-(c) represents vorticity contours of foil, fin and MBS at *St*=0.2. (d)-(f) represents vorticity contours of foil, fin and MBS at *St*=1.0. (a1)-(c1) represents velocity vectors (zoomed-in view) near the wake of foil, fin and MBS at *St*=0.2. (d1)-(f1) represents velocity vectors (zoomed-in view) of near the wake of foil, fin and MBS at *St*=1.0 for *Re*=1000 and A_{max} = 0.05

4.2 Vorticity profiles in the fluid domain and near-wake region

In this section, we examine the vortex behaviour of three different shapes: the fin, the foil, and

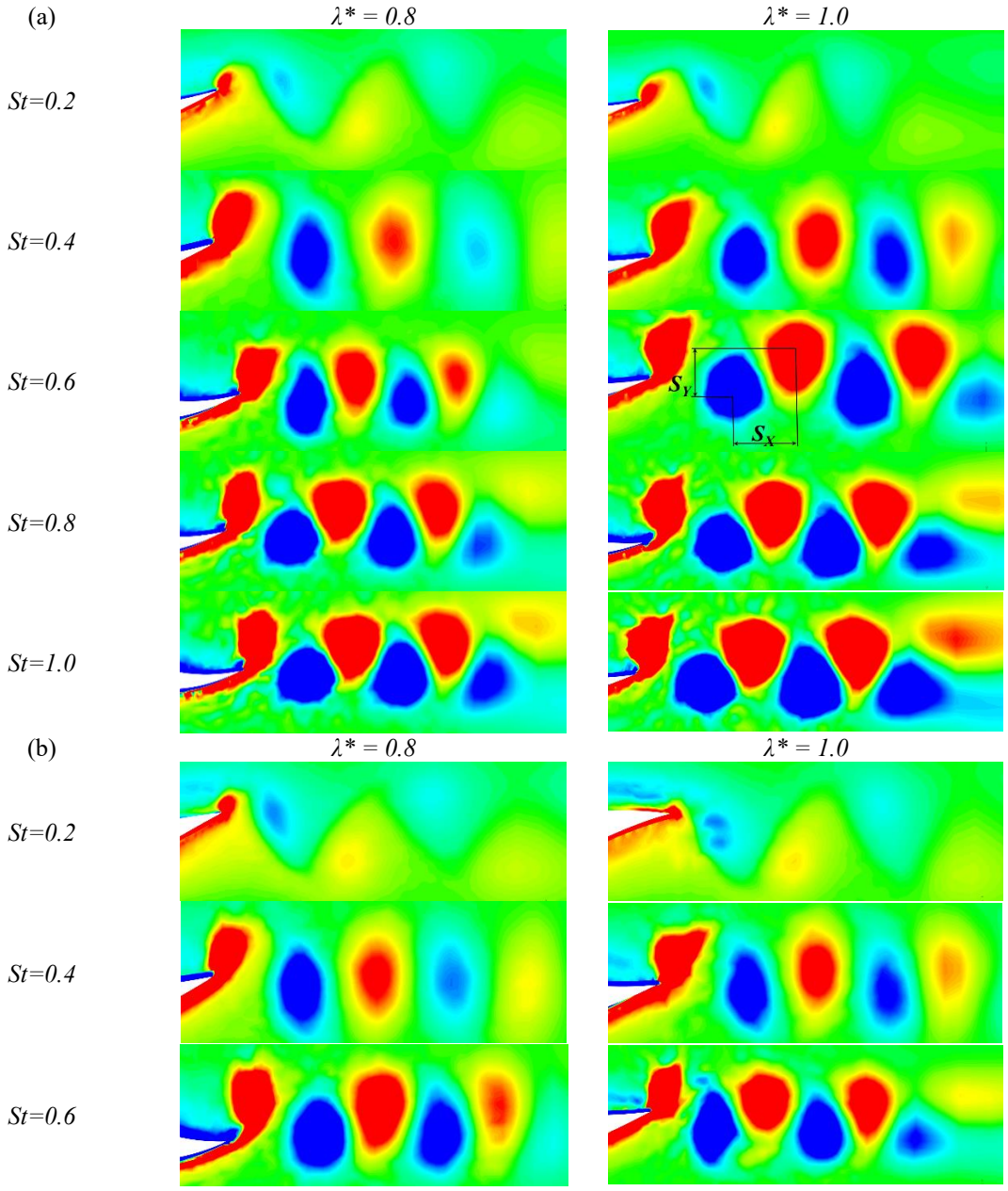

Fig. 14 Instantaneous Vorticity contours for St=0.2, 0.4, 0.6, 0.8 and 1.0 for foil (a) and MBS (b) for λ^*=*0.8 and* λ^*=*1.0 at* A_{max} =0.05 and Re=1000. The streamwise and lateral spacing between the centers of the two consecutive opposite-signed shed vortices are marked as S_X and S_Y, respectively

an MBS, focusing on the vortex pattern that determines thrust or drag generation. The Fig. 12 illustrates the vorticity contour (a-f) and zoomed view of vorticity contour with velocity vectors near the tail (a1-f1) over the foil, fin, and MBS for two St values; one for the lowest (St = 0.2) and

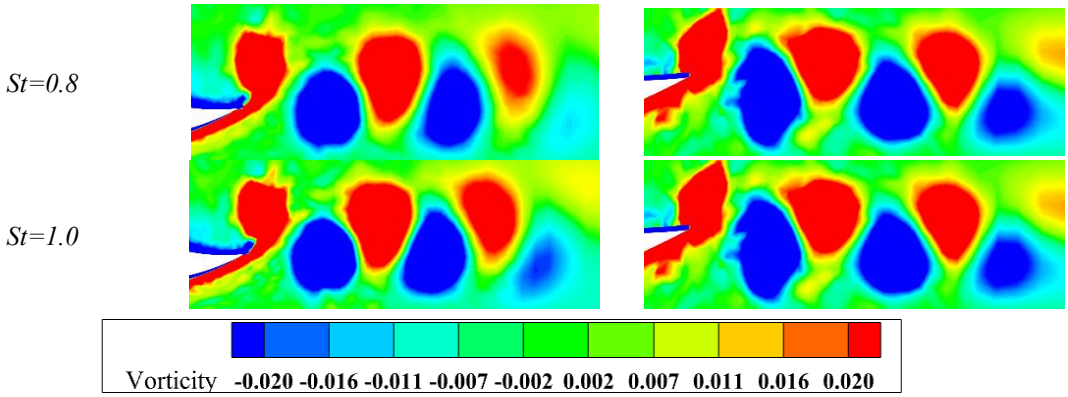

Fig. 14 Continued-

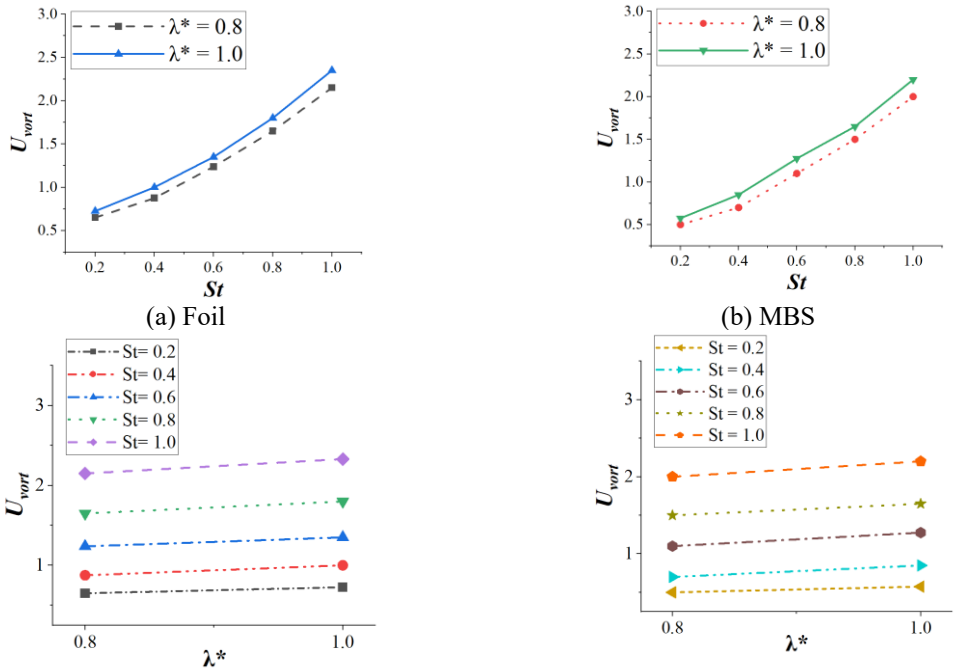

(a) Foil (b) MBS

(c) Foil (d) MBS

Fig. 15 The change in the non-dimensional streamwise velocity of shed vortices, U_{vort} is analyzed for increasing order of *St* (a) and (b) and (c) λ^* (c and d) for foil (a and c) and MBS (b) and (d) at A_{max}=0.05 and *Re*=1000

the other for the highest (*St* = 1.0) at λ*=0.8. It clearly depicts the shedding of positive (CCW) and negative (CW) vortices on either side of the body. Comparing the vortex pattern for all the three profiles at *St*=0.2 as shown in Figs. 12(a)-12(c) the CW vortices formed on the right side and CCW vortices formed on the left side of the foil with respect to the symmetry line (chord line),

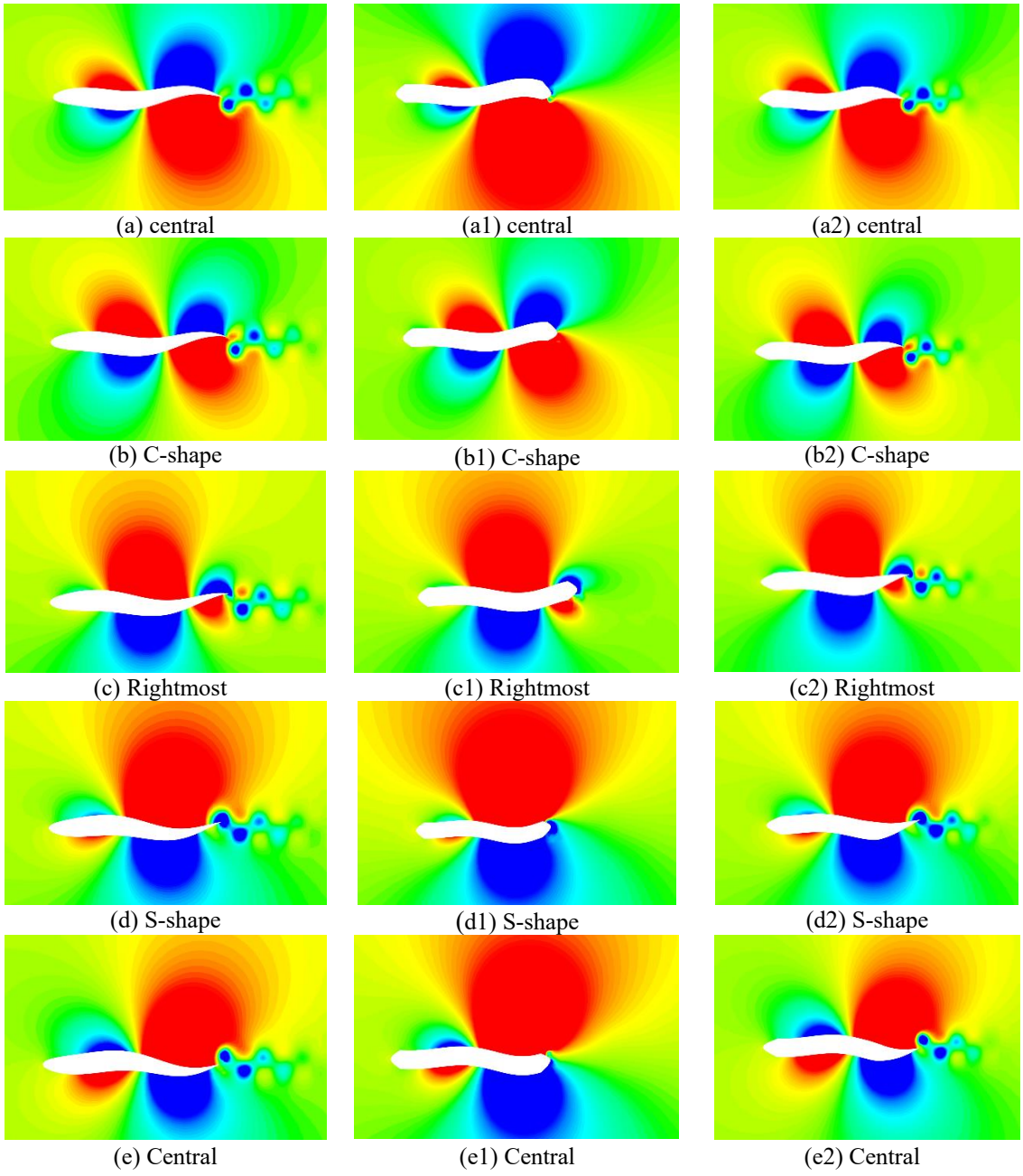

Fig. 16 Instantaneous pressure contours of foil (a)-(h), fin (a1)-(h1), MBS (a2)-(h2) at St=1.0 for Re=1000, λ*=0.8 and A_{max} = 0.05

resembles more like a von Kármán vortex street indicating drag formation as shown in Figs. 17(a) and 17(b) with mean thrust coefficient value in negative zone. Conversely the vortex pattern for foil and MBS at St=1.0 as shown in Figs. 12(d) and 12(f) the CW vortices formed on the left side

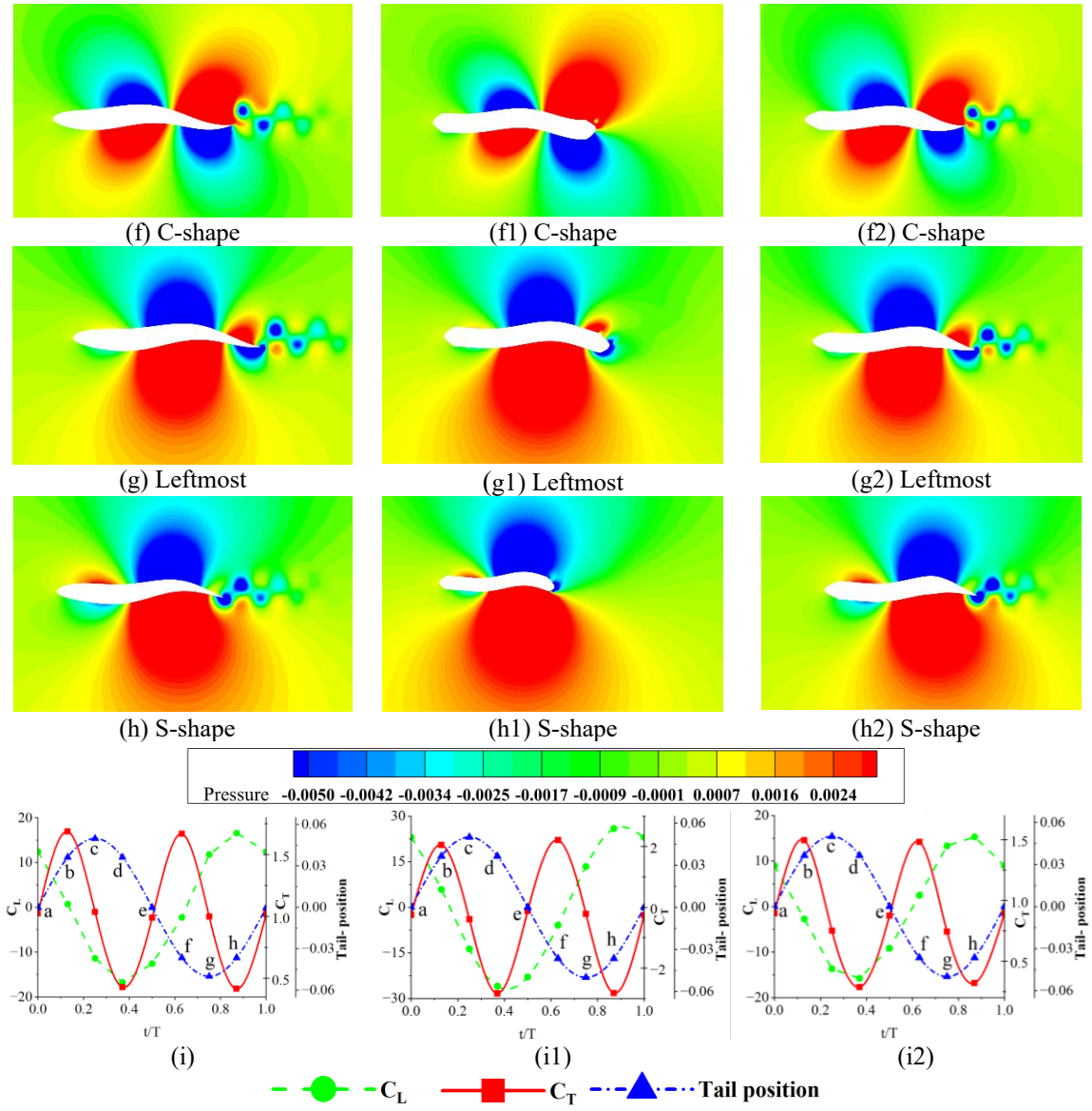

Fig. 16 Continued-

and CCW vortices formed on the right side of the foil with respect to the symmetry line, resembles more like a reverse von Kármán vortex street indicating thrust formation that can be correlated with increasing C_{Tm} value as shown in Figs. 17(a) and 17(b). But looking at the vortex strength, the foil generates higher thrust compared to MBS.

Conversely, in the wake of the fin, for both St=0.2 and at St=1.0, the vortices appear to merge further downstream, forming larger structures, a characteristic phenomenon in bluff body flows (Fallah *et al*. 2022). The irregular distribution of vorticity in the wake, due to merging of the vortices, indicating complex flow interactions, which results in increasing drag with increasing *St,*

can be inferred from Figs. 17(a) and 17(b), the entire C_{Tm} curve falls in negative zone clearly indicating formation of drag. Besides the velocity vectors indicate the direction of fluid jet near the wake which determines thrust or drag formation. For instance at St = 1.0, the foil (refer Fig. 12(d1)) generates a stronger fluid jet in the downstream direction, leading to thrust generation, inferred from higher C_{Tm} in Fig. 17(a).

The same pattern holds for the MBS, though with a slightly lower jet velocity than the foil, as reflected by the lower C_{Tm} in Fig. 17(a). For the fin, the situation is quite different: at St = 1.0, the fin behaves more like a bluff body, generating reverse flow as shown in Fig. 12(e1), resulting in drag. Increasing the St enhances thrust for both the foil and MBS, while it increases drag for the fin. This clearly demonstrates the impact of St on the hydrodynamic characteristics of an anguilliform swimmer. Increasing λ* does have substantial effect on hydrodynamic characteristics. The instantaneous vorticity contours for the foil, fin, and MBS at λ^* = 1.0 for St = 0.2 and St = 1.0 as shown in Figs. 13(a)-13(f) respectively. The vorticity contours and velocity vectors configurations are similar to those observed in the previous case (i.e. λ^* = 0.8). Notably, as shown in Figs. 17(a) and 17(b), the C_{Tm} values for the foil and MBS are higher for λ^* = 1.0 compared to λ^* = 0.8, due to the increased vortex strength at λ* = 1.0. The velocity vectors for λ^* = 1.0 are similar to those for λ^* = 0.8 but exhibit higher jet velocities resulting in a higher C_{Tm} for both the foil and MBS which can be inferred from Fig. 17(b). At higher wavelengths, an anguilliform swimmer produces greater thrust, particularly during the acceleration phase, which aids in escaping predators. However, a significant increase in wavelength leads to larger fluctuations in axial force, limiting the swimmer's ability to effectively use longer wavelengths, as reported by (Du clos *et al*. 2019, Khalid *et al*. 2021). Conversely, the drag force on the fin is greater at λ^* = 1.0 compared to λ* = 0.8, due to the increased strength of the drag-inducing vortices.

4.3 Instantaneous analysis of vortices: Form, dynamics, and intensity

To investigate the vortex shape and the vortex dynamics, the instantaneous vortex pattern for the foil and MBS with increasing *St for* λ* = 0.8 and λ^* = 1.0 is illustrated in Fig. 14. At low St (~ 0.2), the vortices are more spaced out in the streamwise direction, forming a loose and laterally elongated wake structure. The shed vortices appear in a sequential pattern (for St = 0.4), with positive and negative vortices alternating along the centerline of the wake along the streamwise direction. With increasing St (~ 0.6 to 1.0), the vortices become closer, lobed shape and becomes more compact due to higher shedding frequency and start aligning in a slanted arrangement, often appearing in a top-and-bottom configuration relative to the wake centreline (Chao *et al*. 2022).

The interaction between consecutive vortices intensifies, leading to a more robust and organized wake structure that maximizes thrust generation. For both foil and MBS, at St=0.2, negative vortices on the right and positive vortices on the left lead to drag generation. With increasing St, the direction of the vortices reverses, leading to thrust formation as indicated in Figs. 17(a) and 17(b). Increase in λ^* enhances the vortex strength thereby amplifying the hydrodynamic forces for both foil and MBS. Conversely, the flow around the fin does not generate sufficient streamwise momentum to carry the shed vortices downstream. Instead, the vortices interact with the surrounding flow, merging or dissipating rather than being convected as distinct entities (Figs. 12(b) and 12(e)). A formulation connects the vortex dynamics to the foil's motion characteristics is the non-dimensional streamwise velocity of shed vortices, $U_{vort,}$ using the non-dimensional streamwise spacing S_X. This velocity is computed based on the relationship $U_{vort} = St \cdot S_X/A_{max}$,

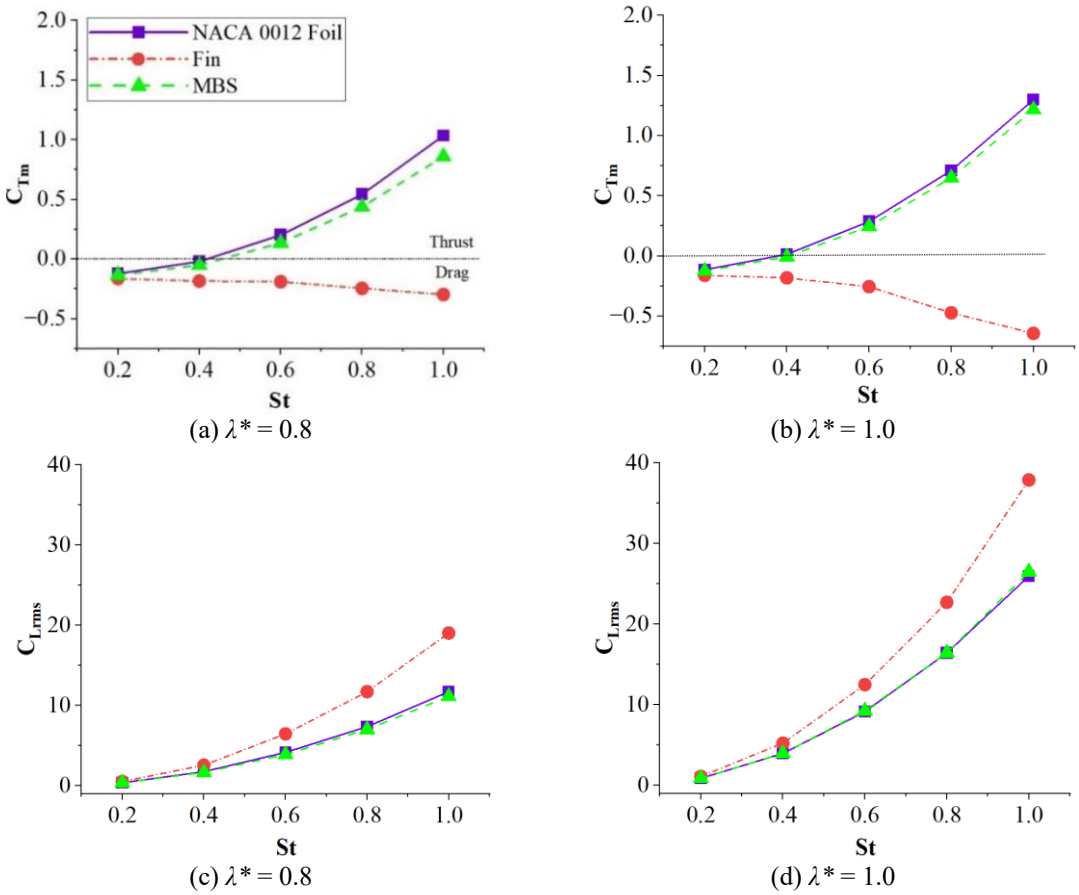

Fig. 17 (a) and (b) Time-averaged thrust coefficient (C_{Tm}), and (c) and (d) RMS value of the lateral force coefficient (C_{Lrms}) at λ* = 0.8 and 1.0, respectively, for the foil, fin, and MBS with increasing Strouhal number at Re = 1000 and A_{max} = 0.05

where S_X represents the spacing between the centers of two consecutive vortices in the streamwise direction (Ohashi and Ishikawa 1972, Thekkethil *et al*. 2018). Likewise S_Y, represents the lateral spacing between the centers of two consecutive vortices.

The spacing S_X decreases with St and increases with λ^* as seen from Fig. 14. The variation of U_{vort} with St (a and b) and λ^*(c and d) are presented in Fig. 15 for foil and MBS respectively. Increase in St increases U_{vort} for both foil and MBS. A higher St implies a greater frequency of undulation, though S_X reduces due to closer spacing of vortices caused by the higher shedding frequency, results in an increase in the transport velocity of the vortices in the streamwise direction as shown in Figs. 15(a) and 15(b). Increase in λ^* results in increasing U_{vort} at all St values for both foil and MBS, as shown in Figs. 15(c) and 15(d). The foil generates a higher U_{vort} than the MBS and hence its thrust generation capacity is moderately higher than the MBS (Figs. 17(a) and 17(b)). A well-tuned U_{vort}, achieved by optimizing parameters such as the St, A_{max} and, λ^* ensures constructive vortex interactions, leading to enhanced thrust. On the other hand it is observed from Fig. 14, the lateral spacing S_Y, increases (the value tending towards $2A_{max}$) with increasing St.

4.4 Pressure fields

As it is known that the pressure differences are generated due to the body undulation which generates a net force imparting momentum to the surrounding fluid, manifested as thrust or lateral force (Liu *et al*. 1996). Figs. 16(a)-16(h), 16(a1)-16(h1) and 16(a2)-16(h2) illustrates the pressure distribution over the foil, fin and MBS respectively at eight different time instants during one undulation time period for A_{max}=0.05, λ^*=0.8, Re=1000 and St=1.0. The sub figures (i, i1 and i2) in Fig. 16 illustrate the time history of one undulation cycle, corresponding to the time instants of the pressure contours relative to the tail position at those moments. The green dashed line, red solid line and blue dashed-dotted line in the time history plot, shows periodic variations of C_L, C_T and tail position, respectively, during one period of undulation. The time instants labelled (a-h) mark critical positions or transitions in the cycle, such as points of maximum C_L, maximum C_T, or changes in the tail's position.

The instantaneous shape of the foil, fin, and MBS shown in Fig. 16 resembles C-like and S-like shapes (Liu *et al*. 1997 and Thekkethil *et al*. 2017). Although this is less apparent in the fin and MBS, a closer examination reveals that they also adopt C and S shapes similar to the foil. The C shape consists of 1 crest (Figs. 16(f), 16(f1) and 16(f2)) or 1 trough (Figs. 16(b), 16(b2) and 16(b3)) whereas the S shape consists of 1-crest and 1 trough in (Figs. 16(d), 16(d1), 16(d2), 16(h), 16(h1) and 16(h2)).

From the pressure contours, it is observed that, high pressure zone near the head and a low pressure zone near the tail are formed on the right side and vice versa on the left side for the first half cycle (Figs. 16(a)-16(c)) and this pattern reverses for second half cycle of undulation (Figs. 16(e)-16(g)). This establishes a pressure difference between the head and tail sections, which influences the thrust and drag generation. If the pressure difference is greater at the tail, it results in thrust; conversely, if it is greater at the head, it leads to drag (Thekkethil *et al*. 2018). Maximum thrust is achieved when there is the greatest growth of momentum in streamwise direction, as shown when the foil, fin, and MBS are in the positions depicted in Figs. 16(b), 16(f), 16(b1), 16(f1), and 16(b2), 16(f2)), respectively. The body profile corresponds to the C-shape. In these positions, the pressure distribution is in such a way that huge mass of fluid is pushed in the downstream direction, resulting in a higher thrust. The corresponding position (b and f) of the tail for maximum C_T is indicated in the time histories as shown in Figs. 16(i), 16(i1), and 16(i2) for the foil, fin and MBS respectively.

Conversely, when the foil, fin, and MBS are in the positions depicted in Figs. 16((d), 16(h), 16(d1), 16(h1), and 16(d2), 16(h2)), respectively, the pressure distribution creates a larger force component acting laterally rather than in the downstream direction corresponds to the S-shape. In this configuration, the pushing zone is primarily oriented laterally, reducing momentum exchange in the downstream direction while increasing it laterally. This results in the maximum lateral force coefficient.

The corresponding positions (d and h) of C_L are marked on the plots in Figs. 16(i), 16(i1), and 16(i2). Additionally, the plots show that the fin generates a larger lateral force coefficient compared to the foil and MBS, which can be correlated with the higher C_{Lrms} value of the fin in Figs. 17(c) and 17(d). The pressure contours of foil, fin and MBS for λ^*=1.0 at these 8 time instants are similar with λ^*=0.8, with slightly higher intensity of pressure. Thus λ^*=1.0 generates a higher C_{Tm} and C_{Lrms} when compared to λ^*=0.8 for the bodies under investigation, except for fin as it generates negative $C_{Tm.}$

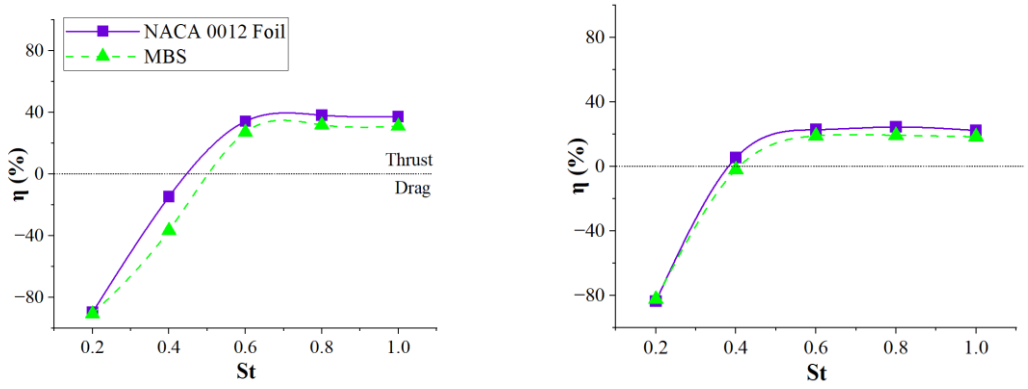

(a) $\lambda^* = 0.8$ (b) $\lambda^* = 1.0$

Fig. 18 (a) and (b)Propulsive efficiency with increasing order of *St* at λ* = 0.8 and 1.0, respectively, for foil and MBS at *Re* = 1000 and A_{max} = 0.05

4.5 Performance metrics

In this section, we discuss the performance of the foil, fin and MBS using thrust and propulsive efficiency as the primary metrics. Thrust generation and propulsive efficiency are key indicators of the hydrodynamic effectiveness of each shape, and understanding how these metrics vary will provide insights into their relative performance.

For *Re* = 1000 and A_{max} = 0.05, the time-averaged thrust coefficient and root mean square (RMS) value of lateral force coefficient at $\lambda^* = 0.8$ and $\lambda^* = 1.0$ are shown in Figs. 17(a) and 17(c) and 17(b) and 17(d), respectively, across a Strouhal number range of *St* = 0.2 to 1, with ΔSt = 0.2, for the foil, fin, and MBS.

The time-averaged thrust coefficient (C_{Tm}) increases with the Strouhal number for both the foil and the MBS, but decreases for the fin. This observation clearly demonstrates that the frequency of undulation is crucial in determining thrust or drag generation. With other conditions kept constant, an increase in *St* enhances thrust for the foil and MBS, while it increases drag for the fin. The increase in C_{Tm} for the foil is closely attributed to its streamlined shape, whereas, the fin's uniform thickness results in increased drag at higher *St*. The C_{Tm} values of the MBS are closely match to those of the foil, despite its uniform mid-section. Conversely, the RMS value of the lateral force coefficient (C_{Lrms}) increases with Strouhal number for all three shapes. Interestingly, the fin experiences a higher lateral force compared to the foil and MBS, indicating that the uniform thickness across the entire body generates higher pressure forces in the lateral direction than streamwise direction. Despite the differences in shape, the C_{Lrms} remains analogous for all non-dimensional frequencies for both the foil and the MBS. The C_{Tm} and C_{Lrms} for λ* = 1.0 is higher than λ* = 0.8 for foil and MBS which clearly demonstrates the increase in wavelength enhances the thrust and lateral force. However, for fin, the C_{Tm} is reducing further and this is accompanied by an increase in C_{Lrms}.

The Fig. 18 illustrates the propulsive efficiency of the foil and MBS for λ^* =0.8 and λ^* =1.0, plotted against increasing *St*. The C_{Tm} for both the foil and MBS is higher for λ^*=1.0 compared to λ^* =0.8 (Figs. 17(a) and 17(b)) across all *St* values. It is interesting to note that the efficiency trend is the opposite: λ^*=0.8 exhibits higher efficiency than λ^*=1.0. This discrepancy arises because, while

λ^*=1.0 produces greater thrust, the net power consumption is significantly higher than λ^*=0.8. This indicates that higher thrust generation at λ^*=1.0 comes at the expense of increased power consumption, resulting in lower efficiency. Thus, foils operating at higher λ^* values generate substantial thrust but with reduced efficiency—a trend previously observed by Thekkethil *et al*. (2018). This supports the observation that natural anguilliform swimmers tend to undulate at wavelengths shorter than their body length during steady-state swimming in their migration phase, while opting for longer wavelengths during accelerated swimming (Khalid *et al*. 2021). For the fin, the entire operating regime falls within the drag-dominated zone. Indeed, the fin generates large lateral force (Figs. 17(c) and 17(d)) by consuming more power. Furthermore, the propulsive efficiency is evaluated in terms of thrust, the fin consistently produces drag across both λ^* and all *St*, resulting in negative efficiency and hence it is not discussed alongside with a foil and MBS. When comparing the efficiency of the foil and the MBS, and closely aligns with the performance of the foil.

5. Conclusions

The foil, fin, and MBS are numerically investigated over a range of Strouhal numbers (*St*) from 0.2 to 1.0, with an interval of 0.2, at two wavelength ratios (λ^* = 0.8 and 1.0). The simulations are conducted at a constant Reynolds number (*Re* = 1000) and maximum non-dimensional amplitude (A_{max} = 0.05).

The key conclusions derived from this study are as follows:

- *Vortex formation*: As the foil reaches the rightmost stopping position with increasing deceleration, there is a rightward-accelerated flow (from left side) near the tail. This flow creates a velocity difference across the right and left sides of the tail tip, leading to the formation of a counter-clockwise (CCW) stopping vortex. As the foil begins moving back towards the left, the change in direction and the resulting pressure difference near the tail tip cause the stopping vortex to grow. Besides, the difference between incoming velocity and backward traveling wave velocity results in formation of an additional vortex called secondary vortex. It merges with the previously formed stopping vortex to form the starting vortex. This vortex stretches, advects and detaches when the foil switches its direction back toward the rightmost position. This detachment transforms the starting vortex into a shed vortex. This sequence of starting and stopping vortices demonstrates how the foil's undulatory motion creates alternating vortex pattern.
- *Vortex characteristics*: As *St* and λ^* increase, the vortex pattern transitions from a von Kármán vortex street to a reverse von Kármán vortex street. At *St*=0.2, the foil and MBS exhibits a von Kármán vortex street, resulting in drag. As *St* increases, the vortex pattern transitions to a reverse von Kármán vortex street, resulting in thrust. In contrast, the fin consistently generates drag across all *St*, due to its complex bluff body vortex behaviour. The vortex velocity, *Uvort*, depends on the spacing between the vortices. With increasing *St*, the streamwise spacing S_X decreases, leading to more compact vortex shedding which increases the *Uvort and strength of vortices*, which enhances thrust generation.
- *Pressure contours:* The pressure contours reveal the instantaneous body shape during the undulation process, which influences the generation of thrust or lateral forces. When the body adopts a C-shape, the pressure distribution pushes a significant mass of fluid downstream, enhancing momentum transfer in the streamwise direction and resulting in higher thrust.

Conversely, when the body transitions to an S-shape, the fluid is primarily pushed laterally, increasing lateral momentum exchange and producing a significant lateral force at that moment.

- *Propulsive Efficiency*: The efficiency trend inversely correlates with thrust generation: $\lambda^* = 0.8$ demonstrates greater efficiency compared to $\lambda^* = 1.0$. Although $\lambda^* = 1.0$ generates higher thrust, it also incurs greater power consumption than $\lambda^* = 0.8$. This indicates that the increased thrust at $\lambda^* = 1.0$ comes at the cost of reduced efficiency due to higher energy demands. These findings align with observations of natural anguilliform swimmers, which tend to use wavelengths shorter than their body length during steady-state swimming.

Our investigation reveals that the efficiency and thrust generation capacity of the MBS closely matches that of the foil. Furthermore, our findings offer new insights into the shape of undulatory body profiles, encouraging further numerical studies to explore their hydrodynamic characteristics that will support the design and development of enhanced undulatory robots/vehicles. Future studies will explore broad range of *Re* values and three-dimensional investigations would gain more insights into undulatory swimming mechanism.

Acknowledgments

This research is funded by IIT Madras under the project New Faculty Seed Grant scheme, grant number (IP23240001OENFSC008977). The authors also thank the Department of Ocean Engineering, IIT Madras, Chennai, India for providing facilities to conduct this research. The authors also extend their gratitude for the high performance computing facility from P. G. Senapathy Centre for Computing Resources, IIT Madras, Chennai, India.

References

Abbasinezhad Fallah, D., Rezazadeh, S., Jalili, H. and Raad, M. (2022), "Numerical investigation of triangular bluff bodies size effect on heat and mass transfer phenomena: internal flow", *J. Braz. Soc. Mech. Sci. Eng*., **44**(5). https://doi.org/10.1007/s40430-022-03526-7.

Abbaspour, M. and Ebrahimi, M. (2015), "Comparative numerical analysis of the flow pattern and performance of a foil in flapping and undulating oscillations", *J. Mar. Sci. Technol*., (Japan), **20**(2), 257-277. https://doi.org/10.1007/s00773-014-0297-7.

Barrett, D., Grosenbaugh, M. and Triantafyllou, M. (1996), "The optimal control of a flexible hull robotic undersea vehicle propelled by an oscillating foil", *Proceedings of the Symposium on Autonomous Underwater Vehicle Technology*, Monterey, CA, USA.

Barrett, D.S., Triantafyllou, M.S., Yue, D.K.P., Grosenbaugh, M.A. and Wolfgang, M.J. (1999), "Drag reduction in fish-like locomotion", *J. Fluid Mech*., **392,** 183-212. https://doi.org/10.1017/S0022112099005455.

Bayat, B., Crespi, A. and Ijspeert, A. (2016), "Envirobot: A bio-inspired environmental monitoring platform", In 2016 Ieee/Oes Autonomous Underwater Vehicles (Auv), 381-386. Ieee.

Borazjani, I. and Sotiropoulos, F. (2009), "Numerical investigation of the hydrodynamics of anguilliform swimming in the transitional and inertial flow regimes", *J. Exp. Biol*., **212**(4), 576-592. https://doi.org/10.1242/jeb.025007.

Chao, L.M., Mahbub, A.M. and Cheng, L. (2022), "Hydrodynamic performance of slender swimmer: Effect of travelling wavelength", *J. Fluid Mech*., **947**. https://doi.org/10.1017/jfm.2022.624.

Crespi, A. and Ijspeert, A.J. (2006), "AmphiBot II: An amphibious snake robot that crawls and swims using

a central pattern generator", *Proceedings of the 9th International Conference on Climbing and Walking Robots (CLAWAR 2006).*

Crespi, A., Badertscher, A., Guignard, A. and Ijspeert, A.J. (2005), "AmphiBot I: An amphibious snake-like robot", *Robot. Auton. Syst*., **50**(4), 163-175. https://doi.org/10.1016/j.robot.2004.09.015.

Crespi, A., Karakasiliotis, K., Guignard, A. and Ijspeert, A.J. (2013), "Salamandra Robotica II: An amphibious robot to study salamander-like swimming and walking gaits", *IEEE T. Robot*., **29**(2), 308-320. https://doi.org/10.1109/TRO.2012.2234311.

Dong, G.J. and Lu, X.Y. (2005), "Numerical analysis on the propulsive performance and vortex shedding of fish-like travelling wavy plate", *Int. J. Numer. Method. Fl.*, **48**(12), 1351-1373. https://doi.org/10.1002/fld.984.

Du Clos, K.T., Dabiri, J.O., Costello, J.H., Colin, S.P., Morgan, J.R., Fogerson, S.M. and Gemmell, B.J. (2019), "Thrust generation during steady swimming and acceleration from rest in anguilliform swimmers", *J. Exp. Biol*., **222**(22). https://doi.org/10.1242/jeb.212464/

Gupta, S., Agrawal, A., Hourigan, K., Thompson, M.C. and Sharma, A. (2022), "Anguilliform and carangiform fish-inspired hydrodynamic study for an undulating hydrofoil: Effect of shape and adaptive kinematics", *Phys. Rev. Fluids*, **7**(9). https://doi.org/10.1103/PhysRevFluids.7.094102.

Gupta, S., Sharma, A., Agrawal, A., Thompson, M.C. and Hourigan, K. (2021b), "Hydrodynamics of a fish-like body undulation mechanism: Scaling laws and regimes for vortex wake modes", *Phys. Fluids*, **33**(10). https://doi.org/10.1063/5.0062304

Gupta, S., Thekkethil, N., Agrawal, A., Hourigan, K., Thompson, M.C. and Sharma, A. (2021a), "Body-caudal fin fish-inspired self-propulsion study on burst-and-coast and continuous swimming of a hydrofoil model", *Phys. Fluids*, **33**(9). https://doi.org/10.1063/5.0061417.

Jellyman, D.J. (1979), "Scale development and age determination in New Zealand freshwater eels (Anguilla spp.)", *New Zealand J. Mar. Freshwater Res*., **13**(1), 23-30. https://doi.org/10.1080/00288330.1979.9515777.

Ji, F. and Huang, D. (2017), "Effects of Reynolds number on energy extraction performance of a two dimensional undulatory flexible body", *Ocean Eng*., **142**, 185-193. https://doi.org/10.1016/j.oceaneng.2017.07.005.

Kern, S. and Koumoutsakos, P. (2006), "Simulations of optimized anguilliform swimming", *J. Exp. Biol*., **209**(24), 4841-4857. https://doi.org/10.1242/jeb.02526.

Khalid, M.S.U., Wang, J., Akhtar, I., Dong, H., Liu, M. and Hemmati, A. (2021), "Why do anguilliform swimmers perform undulation with wavelengths shorter than their bodylengths?", *Phys. Fluids*, **33**(3). https://doi.org/10.1063/5.0040473.

Khalid, M.S.U., Wang, J., Dong, H. and Liu, M. (2020), "Flow transitions and mapping for undulating swimmers", *Phys. Rev. Fluids*, **5**(6). https://doi.org/10.1103/PhysRevFluids.5.063104.

Liu, H., Wassersug, R. and Kawachi, K. (1996), "A computational fluid dynamics study of tadpole swimming", *J. Exp. Biol*., **199**(6), 1245-1260

Liu, H. and Kawachi, K. (1999), "A numerical study of undulatory swimming", *J. Comput. Phys*., **155**(2), 223-247.

Liu, H., Wassersug, R. and Kawachi, K. (1997), "The three-dimensional hydrodynamics of tadpole locomotion", *J. Exp. Biol*., **200**(22), 2807-2819.

Muller, U.K., Van Den Heuvel, B.L.E., Stamhuis, E.J. and Videler, J.J. (1997), "Fish foot prints: morphology and energetics of the wake behind a continuously swimming mullet (Chelon labrosus Risso)", *J. Exp. Biol*., **200**(22), 2893-2906.

Namshad, T., Shrivastava, M., Agrawal, A. and Sharma, A. (2017), "Effect of wavelength of fish-like undulation of a hydrofoil in a free-stream flow", *Sadhana - Academy Proceedings in Engineering Sciences*, **42**(4), 585-595. https://doi.org/10.1007/s12046-017-0619-7.

Ohashi, H. and Ishikawa, N. (1972), "Visualization study of flow near the trailing edge of an oscillating airfoil", *Bull. JSME*, **15**(85), 840-847.

Porez, M., Boyer, F. and Ijspeert, A.J. (2014), "Improved lighthill fish swimming model for bio-inspired robots: Modeling, computational aspects and experimental comparisons", *Int. J. Robot. Res*., **33**(10),

1322-1341. https://doi.org/10.1177/0278364914525811.
Stefanini, C., Orofino, S., Manfredi, L., Mintchev, S., Marrazza, S., Assaf, T., Capantini, L., Sinibaldi, E., Grillner, S., Wallén, P. and Dario, P. (2012), "A novel autonomous, bioinspired swimming robot developed by neuroscientists and bioengineers", *Bioinspiration and Biomimetics*, **7**(2). https://doi.org/10.1088/1748-3182/7/2/025001.
Sun, X., Ji, F. and Huang, D. (2020), "Numerical study of the anguilliform mode of fishlike moving with different leading edge shape in power-extraction regime and propulsive regime", *Renew. Energ.*, **146**, 986-996. https://doi.org/10.1016/j.renene.2019.06.106.
Thekkethil, N., Sharma, A. and Agrawal, A. (2018), "Unified hydrodynamics study for various types of fishes-like undulating rigid hydrofoil in a free stream flow", *Phys. Fluids*, **30**(7). https://doi.org/10.1063/1.5041358.
Van den Thillart, G., Palstra, A. and van Ginneken, V. (2007), "Simulated migration of European silver eel; swim capacity and cost of transport", *J. Mar. Sci. Technol*., **15**, 1-16.
Van Ginneken, V., Antonissen, E., Müller, U.K., Booms, R., Eding, E., Verreth, J. and van den Thillart, G. (2005), "Eel migration to the sargasso: Remarkably high swimming efficiency and low energy costs", *J. Exp. Biol*., **208**(7), 1329-1335. https://doi.org/10.1242/jeb.01524.
Videler, J.J. and Hess, F. (1984), "Fast continuous swimming of two pelagic predators, saithe (pollachius virens) and mackerel (scomber scombrus): A kinematic analysis", *J. Exp. Biol*., **109**.
Videler, J.J. and Wardle, C.S. (1991), "Fish swimming stride by stride: speed limits and endurance", Rev. *Fish Biol. Fisher*., **1**, 23-40.
Wei, C., Hu, Q., Shi, X. and Zeng, Y. (2022), "A comparison for hydrodynamic performance of undulating fin propulsion on numerical self-propulsion and tethered models", *Ocean Eng*., **265**. https://doi.org/10.1016/j.oceaneng.2022.112471.
Xiao, Q., Sun, K., Liu, H. and Hu, J. (2011), "Computational study on near wake interaction between undulation body and a D-section cylinder", *Ocean Eng*., **38**(4), 673-683. https://doi.org/10.1016/j.oceaneng.2010.12.017.
Zhang, D., Pan, G., Chao, L. and Zhang, Y. (2018), "Effects of Reynolds number and thickness on an undulatory self-propelled foil", *Phys. Fluids*, **30**(7). https://doi.org/10.1063/1.5034439.

MK